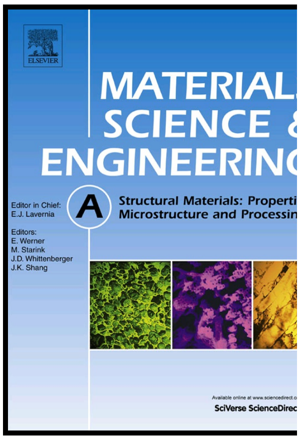

www.elsevier.com/locate/msea

Processing and properties of topologically optimised biomedical Ti-24 Nb-4Zr-8Sn scaffolds manufactured by selective laser melting

Y.J. Liu, X.P. Li, L.C. Zhang, T.B. Sercombe

PII: S0921-5093(15)30142-8
DOI: http://dx.doi.org/10.1016/j.msea.2015.06.088
Reference: MSA32526

To appear in: *Materials Science & Engineering A*

Received date: 7 May 2015
Revised date: 23 June 2015
Accepted date: 26 June 2015

Cite this article as: Y.J. Liu, X.P. Li, L.C. Zhang and T.B. Sercombe, Processing and properties of topologically optimised biomedical Ti-24 Nb-4Zr-8Sn scaffold manufactured by selective laser melting, *Materials Science & Engineering A* http://dx.doi.org/10.1016/j.msea.2015.06.088

Processing and properties of topologically optimised biomedical Ti-24Nb-4Zr-8Sn scaffolds manufactured by selective laser melting

Y. J. Liu[a], X. P. Li[b], L. C. Zhang[a] and T. B. Sercombe[b*]

[a]*School of Engineering, Edith Cowan University,270 Joondalup Drive,*

Joondalup, Perth, WA 6027, Australia

[b]*School of Mechanical and Chemical Engineering, The University of Western Australia, 35 Stirling Highway, Crawley, Perth, WA 6009, Australia*

[*]Corresponding author. E-mails: tim.sercombe@uwa.edu.au

Abstract

This study investigated the effect of the processing parameters on the quality and mechanical properties of a biomedical titanium alloy (Ti–24Nb–4Zr–8Sn) scaffolds fabricated by selective laser melting. Optimal manufacturing parameters were then determined through analysing the pores distribution, geometrical accuracy and the mechanical properties of the produced components. The evaporation of tin during the process is thought to be the main cause of pore generation at higher incident energy densities. Using the optimal processing conditions, the strength of the scaffold reached 51MPa at a scaffold density of <1g/cm^3 and a high solid strut relative density of ~99.3%. Fracture surface analysis found that the main reason for strut early failure was the weaknesses of struts caused by the presence of pores as well the thickness of strut and internal unmelted powders.

Keywords: Selective laser melting; Ti-24Nb-4Zr-8Sn; mechanical behaviours, porous materials

1. Introduction

Driven by the increasing number of joint diseases related to an aging population and obesity, it has been estimated that the required number of total hip replacements and total knee arthroplasties will increase by 174% and 673% by 2030, respectively[1]. These artificial joints have been employed to reduce the suffering and improve the patient's quality of life. The material from which the implant is fabricated from should have sufficient mechanical strength to sustain the loads to which they are exposed [2], so that the risk of failure and consequential painful revision surgery is minimised [3]. Excellent biocompatibility, as well as a low modulus and no cytotoxicity, are key requirements, especially in load-bearing applications [4-7]. Currently, the three most commonly used load-bearing implant materials are stainless steel, CoCr alloys and titanium [8-10].With some unique properties, such as high strength and corrosion resistance and low modulus [11], titanium alloys are more preferable than CoCr alloys and stainless steel in orthopaedic applications. Mismatch in stiffness between an implant and the surrounding bone can cause stress shielding, which often results in implant loosening and the need for revision surgery [12]. Ti–24Nb–4Zr–8Sn (abbreviated hereafter as Ti2448), with a nominal chemical composition of 24% niobium, 4% zirconium and 8% (all in weight percent) [11], has a significantly lower modulus of ~42-50GPa compared with other conventional titanium alloys (~100-120 GPa) [5]. It has the potential to improve the performance of implant with its low modulus, high biocompatibility, strength and corrosion resistance [13-15].

However, the modulus of Ti2448 alloy (42-50GPa) must be reduced further if it is to match the modulus of bone (4-30GPa) [16, 17]. One common method to reduce the modulus of a material is to introduce porosity into the structure [18-20]. Porous materials play a key role in bone tissue engineering applications, due to their low modulus coupled with the possibility of enhanced biological fixation through bone cell in-growth [21].

The geometric freedom offered by additive manufacturing technologies such as Selective Laser Melting (SLM) are being considered as one of the most advantageous methods for fabricating the complicated porosity structure of an artificial bone implant [22-24]. During SLM process, a high-intensity laser beam selectively scans a thin powder bed, melting the metal particles, which solidify to form a solid layer. The build platform then moves down by the thickness of one layer (typically 50-100μm), a new layer of powder is deposited on top and the process continues until the part is complete. One of the key advantages of selective laser melting is its ability to produce near-full density metallic parts [25-27] with a high degree of geometrical complexity without the need for any tooling or machining [28]. Recent work has coupled topology optimisation with SLM to produce light-weight scaffolds with high specific strength and stiffness [29]. However, this work was performed with Ti-6Al-4V, which has approximately twice the modulus of Ti2448 and therefore requires significantly higher levels of porosity (and therefore lower strength) to match the stiffness of bone. Therefore, enhanced implants may be possible by coupling the latest generation Ti2448 alloy with complex scaffolds made possible by the geometric freedom of SLM.

Scan speed plays a key role among all the processing parameters for the density of the parts [30-33]. Therefore, an understanding of the process mechanisms and effects of process parameters are significant for the future development of implants. This paper investigates the effect of the SLM processing conditions on the quality and properties of complex high-strength and high-ductility Ti2448 scaffolds. The suitable manufacturing parameters can be obtained through analyses of the microstructure and the mechanical properties of the produced components.

2. Experimental

The powder used in the work was a low modulus Ti-24Nb-4Zr-8Sn (Ti2448) alloy that had been produced using electrode induction melting gas atomization (EIGA) by TLS, Germany. The composition of the powder is summarised in Table. 1, while the morphology is shown in Fig. 1 (a), and shows that the powder is nearly spherical. The nominal powder size was +45, -106μm, with the actual distribution shown in Fig. 1 (b). A Realizer SLM100 machine, equipped with a 200W Yb:YAG fibre laser with a spot size of ~40μm,was employed in this work. Prior to building, the chamber was purged using a high purity argon atmosphere until with oxygen content was less than 0.1%. Scaffold structures consisting of 3×3×3 unit cells with 15% solid fraction (i.e. 85% porosity) (Fig. 2(a)) were manufactured by SLM with a laser power of 175W and laser scan speeds of between 500 and 1500mm/s. Each unit cell size was 3.33mm×3.33mm×3.33mm.The design of the scaffold structure has been reported elsewhere [19, 21, 34]. The scanning strategy used was for the laser to initially scan the contours of each layer and then use a raster fill. The direction of the fill lines was rotated 90° between layers. Fig. 2 (b) shows the laser path of a single section of one layer. The black lines represent the outer boundary of the geometry and the red lines are the path that the laser took to produce the outline. This line was offset 60µm from the outer boundary of the geometry (black line) to account for the radius of the melt pool. The fill lines are shown in green and the distance between these was 100µm. The structures of the as-produced part were examined using a ZeissVersa520 Micro-CT. The Micro-CT was performed using at an accelerating voltage of 160 kV and current of 62.5µA with a voxel size of 4µm. Projections (2001 at 3s exposure time) were collected on a charge-coupled device detector. Micro CT images were then reconstructed using XMReconstructor software. For each laser scan speed, three samples were scanned. Avizo 8.0 was used to analyse the Micro-CT 3D raw data and determine the pore distribution. From this, the relative density of solid and the thickness of strut could be calculated. Compression testing of the SLM produced Ti2448 scaffolds was carried out using an Instron 5982 machine. Samples were compressed in a direction parallel to building direction (i.e. Z-direction of the SLM-produced samples) using a strain rate of 0.5mm/min. The reported properties are the average of five individual samples. The fracture surfaces were observed using a Zeiss 1555 scanning electron microscope (SEM) at an accelerating voltage of 15KV.

3. Results

A single projection vertically through the midpoint of a unit cell is shown in Fig 3 for speeds between 500 and 1500 mm/s. It is apparent that the amount of porosity (black) decreases significantly between 500mm/s and 750mm/s and then is relatively constant. Fig. 4 shows the location and distribution of the porosity within unit cell, which is mostly spherical. Similar to Fig. 3, there is an obvious decrease in the volume of porosity between 500 and 750mm/s. The size distribution of the pores along with the average size and overall density of the structures are shown in Figure 5. The average pore size is the diameter of a sphere which has the same volume as the measured pore. Due to the resolution of the micro CT data, the minimum detectable pore size was 4μm. Fig. 5 (a) shows distribution of pore size for the five laser scan speeds used while Fig. 5 (b) shows the changes of the average pore size and the relative density with laser speeds. The mode pore size is between 10 and 20μm for laser scan speeds. At larger pore sizes (>50μm), with the exception of the 500mm/s samples, there is little difference between pore distribution. At 500mm/s scan speed, there is a significant increase in the amount of large pores present. This increase in the number of large pores affects both the average pore size and relative density (Fig 5(b)). There is a clear density increase when the laser scan speed is increased from 500mm/s to

750mm/s, at which point the samples are >99% dense. Further increasing the laser speed does not significantly increase the density, which plateaus at just over 99%.The average pore size decreases sharply between 500 and 750mm/s, before increasing slowly as the scan speed is increased further.

Fig. 6 shows the top view (a) and side view (b) of samples produced at all 5 speeds. It is apparent that the upwards facing surfaces are considerably smoother than the downward facing ones. The thickness of the struts has been measured both in the X-Y plane and build (Z) plane, and the results summarised in Fig 7. It is apparent that the scan speed has a much smaller effect on the thickness in the X-Y plane than in the Z direction. In addition, the size of the arms is both bigger and more variable in the build direction. As a result of the change in strut dimension in the build direction, the single unit volume also decreases with increasing scan speed, Fig. 7(b).

The mechanical properties of Ti2448 scaffold structures at different laser scan speed were measured and plotted against the Z plane strut thickness in Fig. 8 (a) and the density of the structure in Fig. 8 (b). Typical stress-strain curves are shown in Fig. 8 (c). Initially as the scan speed decreases, there was a sharp increase in both Z plane strut thickness and density. The strength also increased rapidly. Decreasing the speed from 750 to 500mm/s saw a significant increase in overall density of the scaffold structure (ie an increase in the volume of material) but only a modest (~2MPa) increase in strength. The stress-strain curves reveal smooth loading until the point where the first failure occurs (arrowed) at which a rapid drop in the load occurs. Subsequent deformation is accompanied by a series of these drops in load.

Fig. 9 shows the morphology of the 1000mm/s scaffold after testing to just beyond the first drop in load (see Fig. 8(b). It shows the location of the failed strut is in the X-Y plane (circled in Fig. 9a) and is also clearly seen in the 3D vertical view (Fig.9(b)). The location of first fractured failed strut at all scan speeds was the same – that is in the horizontal (X-Y) plane.

The fracture surfaces of the struts were examined using SEM and typical fractographs are shown in Fig. 10. At 500mm/s (Fig. 10 (a)), the surface contains several large pores along with significant areas of dimple fracture. When the laser speed is increased to 750mm/s or 1000mm/s (Fig 10 (b) and (c)), quasi-cleavage facets are present along with area of dimple fracture. At the faster speeds, (Fig. 10 (d) and (e)) unmelted particles were present on the surface.

4. Discussion

In general, the energy density input for an SLM component is given by :

$$Energy\ Densiy\ = \frac{Laser\ Power}{scan\ speed\ x\ scan\ spacing\ x\ layer\ thickness} \qquad [35]$$

In this work, laser power, scan spacing and layer thickness were all kept constant at 175W, 100µm and 50µm, respectively and therefore the energy density is proportional to $\frac{1}{scan\ speed}$.

It is apparent from Figures 3 to 5 that at the high energy density (slowest scan speed) there is an increase in the size and volume of porosity. This was not expected as an increase in energy density normally results in an improvement in density from more complete melting [36]. In this case, however, complete melting appears to occur for all speeds less than 1250mm/s and therefore is it possible that it is an excess in energy that is causing the porosity. It is known that low scan speeds can result in a poor quality melt trace as a result of Marangoni flow [37]. However, this porosity would tend to be irregular, and not spherical as seen in Fig 3(a). Another possibility is the vapourisation of metal, which is known to occur during laser processing [38-40]. The boiling point of Ti, Nb, Zr and Sn are approximately 3290, 4740, 4400 and 2600°C, respectively, while the melting point of Ti2448 is estimated at ~1800°C. Hence, given that in order to produce a high density part, a significant superheat of the melt pool is usually required, it is possible that significant vapourisation of the Sn is occurring. Since the surface of melt pool solidifies rapidly, the Sn vapour becomes trapped inside the melt, resulting in the formation of a spherical vapour bubble. If the porosity was indeed caused by vapourisation, then as the energy density increased (laser scan speed decreased) then the peak temperature of the melt pool would rise, leading to more vapourisation and higher porosity, which is what is shown in both Fig. 3(a) and Fig. 4 (a).

Another possible mechanism for the porosity is that the Argon atmosphere may becoming trapped in the melt as a result of the rapid heating and cooling of the processes. However, at slower laser scan speeds the material is molten for longer and therefore it would be expected that more Ar would diffuse out of the melt pool results in less porosity.

It is apparent that the laser scan speed is having a significant effect on the size of the struts in the build (Z) direction with slower speeds resulting in a thicker strut (Fig. 9a) and therefore a greater unit cell volume (Fig. 9b). In the X-Y plane (ie the plane of a single layer), the scan speed has only a minor influence on the strut size. In the X-Y plane, the size of the strut is largely determined by the positional accuracy of the laser delivery optics as well as the width of the melt pool that is created. The latter is a function of the energy density, with a wider melt pool expected at slow scan speed [41]. Since the beam compensation was kept constant, the wider melt pool at slower scan speeds will result in a thicker strut.

The temperature increase of the material during SLM is determined by the competition between the input laser energy density and the rate of heat conduction through the underlying material. When building inclines, the downwards facing surface contains overhangs. These are regions which are built on powder – that is there is no previously built solid material underneath. Since the heat conduction of the powder is much lower than that of solid [42], the material in the overhangs becomes superheated, which will lead to significant melting of the powder below the layer. This caused “Z-growth” and is likely to be the cause of increase in both the size and surface roughness of the struts in the build direction.

The thickness of strut and hence the volume of unit cell are known main factors to affect the mechanical properties of scaffolds structures [43, 44]. This relationship between the strut thickness and strength is shown in Fig. 8(a). It is clear that the strength of the scaffolds increases sharply with the thickness of the strut in the Z plane. Furthermore, for the 500 mm/s, 750mm/s and 1000 mm/s groups, the struts fractured (which manifests by a small, sudden drop in the stress) at the maximum stress. In contrast, for laser scan speeds of 1250mm/s and 1500mm/s the stress continued to rise even after the first strut had broken (the location of the first strut failure is arrowed in Fig 8(c). This may be explained by that the fact that at the faster speeds, the strut dimensions are much more variable (Fig. 7) due to insufficient laser energy and therefore failure may occur at the locally thin areas [32]. Furthermore, porosity [31, 45] and unmelted powder [33] in solid strut are known to be important factors in determining strength and although the porosity increase slightly, the presence of unmelted particles at the faster scan speeds will be contributing to the lower strength of the scaffold.

In general the properties are determined by the density of the unit cell. However, at a laser scan speed of 500mm/s the significant increase in density does not result in a commensurate level of strengthening. The reason for this may be two fold. Firstly, the significant increase in porosity at this scan speed will act to decrease the strength. Secondly, the additional volume of material that is produced (which is primarily a result of Z-growth which increases the strut dimension in the build direction) may not be effectively contributing to the load sharing capabilities of the structure and therefore be not increasing the strength.

The fracture position, indicated by an arrow in Fig. 8 (c) occurs in the arms in the X-Y plane. The crack normally occurred in the strut at the thinnest section as is shown in Fig. 9. It has been shown that this part of the unit cell carries the highest tensile stresses and that the surface roughness has a direct consequence on the failure site [34]. This previous work was done on scaffolds made using Ti-6Al-4V, which exhibited low (<3%) as-processed ductility and therefore is more susceptible to tensile failure. For Ti2448 the as built ductility is approximately 14% [31]. Despite this increased ductility, the failure still appears to occur in the horizontal arms which carry the tensile load.

5. Conclusions

Porous structures consisting of 3×3×3 unit cells with 15% solid fraction were manufactured by selective laser melting with five different lasers scan speed from 500mm/s to 1500mm/s. Scaffolds parts with near full density of solid strut (>99%) have been obtained at a laser power of 175 W and with a scan speed range of 750-1000 mm/s^{-1}. The shape and amount of pores inside the solid strut of scaffold were mapped using Micro CT, which clearly showed the difference of distribution of pores with different laser scan speeds. The evaporation of tin during SLM process it thought to be a major contributor to the increase in porosity that occurs at the slower scan speeds. The scan speed also had an influence on the size of the struts produced, however the effect was significant only in the build (Z) direction. The compression test result showed that 750mm/s group had excellent mechanical properties performance with low solid-section density. Fracture surface analysis showed that the main reason for strut early failure was the weakness of struts, including variable thickness of strut, pores and unmelted powders inside solid strut parts.

Acknowledgments

This work was supported by the Australian Research Council (ARC) Discovery Project DP130103592 and DP110101653. The authors also acknowledge the facilities, and the scientific and technical assistance of the Australian Microscopy & Microanalysis Research Facility at the Centre for Microscopy, Characterisation & Analysis, The University of Western Australia, a facility funded by the University, State and Commonwealth Governments.

.

Reference

[1] S.M. Kurtz, K.L. Ong, J. Schmier, F. Mowat, K. Saleh, E. Dybvik, J. KÃĪrrholm, G. Garellick, L.I. Havelin, O. Furnes, The Journal of Bone & Joint Surgery, 89 (2007) 144-151.

[2] D.W. Hutmacher, T. Schantz, I. Zein, K.W. Ng, S.H. Teoh, K.C. Tan, Journal of biomedical materials research, 55 (2001) 203-216.

[3] M. Long, H. Rack, Biomaterials, 19 (1998) 1621-1639.

[4] S. Hao, L. Cui, D. Jiang, X. Han, Y. Ren, J. Jiang, Y. Liu, Z. Liu, S. Mao, Y. Wang, Science, 339 (2013) 1191-1194.

[5] Y. Hao, S. Li, S. Sun, C. Zheng, Q. Hu, R. Yang, Applied Physics Letters, 87 (2005) 091906-091906-091903.

[6] W. Teng, T.J. Long, Q. Zhang, K. Yao, T.T. Shen, B.D. Ratner, Biomaterials, (2014).

[7] M. Tanaka, M. Takemoto, S. Fujibayashi, T. Kawai, S. Yamaguchi, T. Kizuki, T. Matsushita, T. Kokubo, T. Nakamura, S. Matsuda, Journal of Materials Science: Materials in Medicine, 25 (2014) 635-643.

[8] S. Mändl, J. Lutz, C. Díaz, J. Gerlach, J. García, Surface and Coatings Technology, 239 (2014) 116-122.

[9] X. Hu, K.G. Neoh, J. Zhang, E.-T. Kang, Journal of colloid and interface science, 417 (2014) 410-419.

[10] D. Gu, Y.-C. Hagedorn, W. Meiners, G. Meng, R.J.S. Batista, K. Wissenbach, R. Poprawe, Acta Materialia, 60 (2012) 3849-3860.

[11] Y. Hao, S. Li, S. Sun, C. Zheng, R. Yang, Acta Biomaterialia, 3 (2007) 277-286.

[12] C. Engh, J. Bobyn, A. Glassman, Journal of Bone & Joint Surgery, British Volume, 69 (1987) 45-55.

[13] K. Zheng, X. Li, J. Fu, X. Fan, P. Wang, Y. Hao, S. Li, H. Fan, Z. Guo, Journal of Materials Science: Materials in Medicine, 22 (2011) 1579-1588.

[14] J. Cui, Y. Hao, S. Li, M. Sui, D. Li, R. Yang, Physical review letters, 102 (2009) 045503.

[15] J. Li, S. Li, Y. Hao, H. Huang, Y. Bai, Y. Hao, Z. Guo, J. Xue, R. Yang, Acta Biomaterialia, 10 (2014) 2866-2875.

[16] M. Geetha, A. Singh, R. Asokamani, A. Gogia, Progress in Materials Science, 54 (2009) 397-425.

[17] J.-Y. Rho, L. Kuhn-Spearing, P. Zioupos, Medical engineering & physics, 20 (1998) 92-102.

[18] Y.C. Chai, S. Truscello, S.V. Bael, F.P. Luyten, J. Vleugels, J. Schrooten, Acta Biomaterialia, 7 (2011) 2310-2319.

[19] V.J. Challis, A.P. Roberts, J.F. Grotowski, L.-C. Zhang, T.B. Sercombe, Advanced Engineering Materials, 12 (2010) 1106-1110.

[20] A. Bandyopadhyay, F. Espana, V.K. Balla, S. Bose, Y. Ohgami, N.M. Davies, Acta Biomaterialia, 6 (2010) 1640-1648.

[21] S. Kujala, J. Ryhänen, A. Danilov, J. Tuukkanen, Biomaterials, 24 (2003) 4691-4697.

[22] J. Biemond, G. Hannink, N. Verdonschot, P. Buma, Journal of Materials Science: Materials in Medicine, 24 (2013) 745-753.

[23] M. de Wild, R. Schumacher, K. Mayer, E. Schkommodau, D. Thoma, M. Bredell, A. Kruse Gujer, K.W. Grätz, F.E. Weber, Tissue Engineering Part A, 19 (2013) 2645-2654.

[24] S. Van Bael, Y.C. Chai, S. Truscello, M. Moesen, G. Kerckhofs, H. Van Oosterwyck, J.-P. Kruth, J. Schrooten, Acta Biomaterialia, 8 (2012) 2824-2834.

[25] H. Attar, M. Bönisch, M. Calin, L.-C. Zhang, S. Scudino, J. Eckert, Acta Materialia, 76 (2014) 13-22.

[26] H. Attar, M. Bönisch, M. Calin, L. Zhang, K. Zhuravleva, A. Funk, S. Scudino, C. Yang, J. Eckert,

Journal of Materials Research, 29 (2014) 1941-1950.

[27] J.-P. Kruth, L. Froyen, J. Van Vaerenbergh, P. Mercelis, M. Rombouts, B. Lauwers, Journal of Materials Processing Technology, 149 (2004) 616-622.

[28] A. Roberts, G. Grayson, V. Challis, L. Zhang, J. Grotowski, G. Schaffer, T. Sercombe, Acta Materialia, 59 (2011) 5257-5265.

[29] V.J. Challis, X. Xu, L.C. Zhang, A.P. Roberts, J.F. Grotowski, T.B. Sercombe, Materials & Design, 63 (2014) 783-788.

[30] B. Vandenbroucke, J.-P. Kruth, Rapid Prototyping Journal, 13 (2007) 196-203.

[31] L. Zhang, D. Klemm, J. Eckert, Y. Hao, T. Sercombe, Scripta Materialia, 65 (2011) 21-24.

[32] L. Zhang, T. Sercombe, Key Engineering Materials, 520 (2012) 226-233.

[33] H. Attar, M. Calin, L. Zhang, S. Scudino, J. Eckert, Materials Science and Engineering: A, 593 (2014) 170-177.

[34] T.B. Sercombe, X. Xu, V. Challis, R. Green, S. Yue, Z. Zhang, P.D. Lee, Materials & Design, (2014).

[35] A. Simchi, Materials Science and Engineering: A, 428 (2006) 148-158.

[36] J.-P. Kruth, G. Levy, F. Klocke, T. Childs, CIRP Annals-Manufacturing Technology, 56 (2007) 730-759.

[37] I. Yadroitsev, P. Bertrand, I. Smurov, Applied surface science, 253 (2007) 8064-8069.

[38] K.A. Mumtaz, P. Erasenthiran, N. Hopkinson, Journal of Materials Processing Technology, 195 (2008) 77-87.

[39] J. Hu, H.-L. Tsai, International Journal of Heat and Mass Transfer, 50 (2007) 833-846.

[40] F. Verhaeghe, T. Craeghs, J. Heulens, L. Pandelaers, Acta Materialia, 57 (2009) 6006-6012.

[41] I. Yadroitsev, A. Gusarov, I. Yadroitsava, I. Smurov, Journal of Materials Processing Technology, 210 (2010) 1624-1631.

[42] H.-P. Klein, M. Groll, International Journal of Hydrogen Energy, 29 (2004) 1503-1511.

[43] S. Van Bael, G. Kerckhofs, M. Moesen, G. Pyka, J. Schrooten, J.-P. Kruth, Materials Science and Engineering: A, 528 (2011) 7423-7431.

[44] B. Gorny, T. Niendorf, J. Lackmann, M. Thoene, T. Troester, H. Maier, Materials Science and Engineering: A, 528 (2011) 7962-7967.

[45] R. Li, J. Liu, Y. Shi, M. Du, Z. Xie, Journal of Materials Engineering and Performance, 19 (2010) 666-671.

Table

Table 1. Summary of the characteristics of the Ti-24Nb-4Zr-8Sn powder

Composition (wt %)						Particle size (µm)			Flowability (s/50g)	Apparent density (%)
Ti	Nb	Zr	Sn	O	N	d_{10}	d_{50}	d_{90}	20.5	57.8
Bal	23.2	3.85	8.1	0.15	<0.005	43	69	106		

Figure Captions

Fig. 1 (a) Morphology and (b) particle size distribution of the as-received Ti-24Nb-4Zr-8Sn powder used for selective laser melting.

Fig. 2 (a) Orientation of the optimised scaffolds structure relative to the building direction (Z axis) and scanning direction (X-Y plane), the size of sample was 10mm×10mm×10mmwith 27 single cell unit together, (b) A schematic illustration of laser scan tracks including inner contour, outer contour and hatch lines.

Fig. 3 Single projection Micro CT image of the middle of a single unit cell with a scan speed of (a) 500mm/s; (b) 750mm/s; (c) 1000mm/s; (d) 1250mm/s and (e) 1500mm/s. At 500mm/s there was a greater volume of pores (black areas) than at the other speeds.

Fig. 4 Visualisation of the pore distribution inside of solid strut part with different scan speeds; (a) 500mm/s; (b) 750mm/s; (c) 1000mm/s; (d) 1250mm/s and (e) 1500mm/s.

Fig. 5 Pore distribution, average pore size and the relative density in solid strut of Ti-24Nb-4Zr-8Sn scaffolds with different laser scan speeds: (a) the distribution of pores size and amount, (b) average pore size and the relative density.

Fig. 6 Top view and side view of single cell unit produced at different laser scan speeds. (a) top view of single unit with the uniform smooth strut thickness, (b) side view of single unit with a large rough surface.

Fig. 7(a) The thickness of strut in the X-Y plane and Z plane,(b) the volume of a single unit cell at different scan speeds. Clearlt the scan speed has a significant effect on the strut in the Z (vertical) direction, which causes an overall increase in cell volume.

Fig. 8 Compression test performance of Ti2448 scaffolds as a function of (a) Z plane strut thickness (μm) and (b) density (g/cm^3). In (c) typical compressive stress- strain curves are shown, with the arrows indicating the location of the first strut failure.

Fig. 9 Visualisation of the deformed SLM-processed Ti-24Nb-4Zr-8Sn scaffolds: (a) the middle plane of cells showing the location of the failure (black circle) and (b) a higher magnification view of the crack.

Fig.10 SEM microstructures of fracture surface: (a) 500mm/s groups; (b) 750mm/s groups; (c) 1000mm/s groups;(d) 1250mm/s groups; (e) 1500mm/s groups.

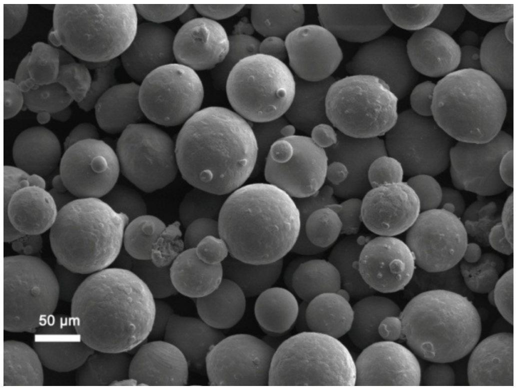

(a)

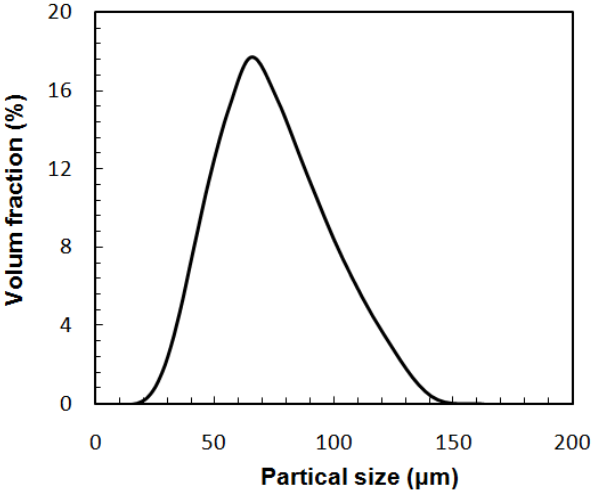

(b)

Fig. 1. Y.J. Liu *et al*

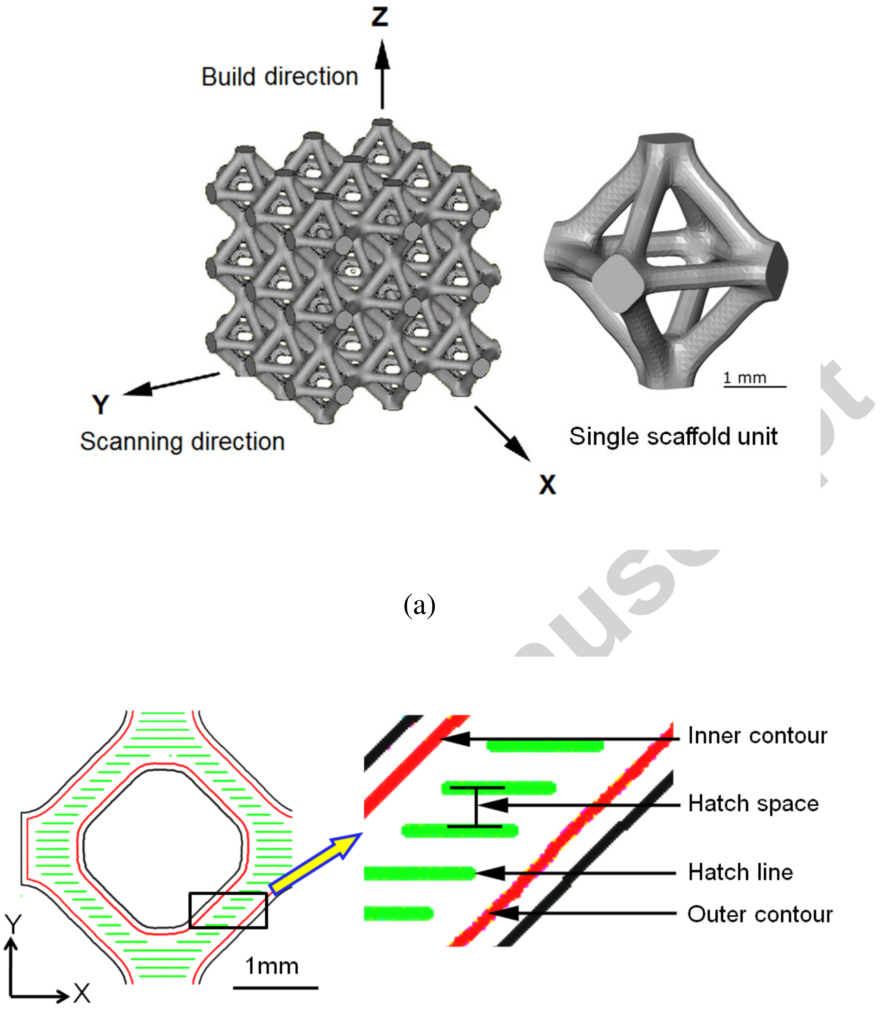

(a)

(b)

Fig. 2. Y.J. Liu *et al*

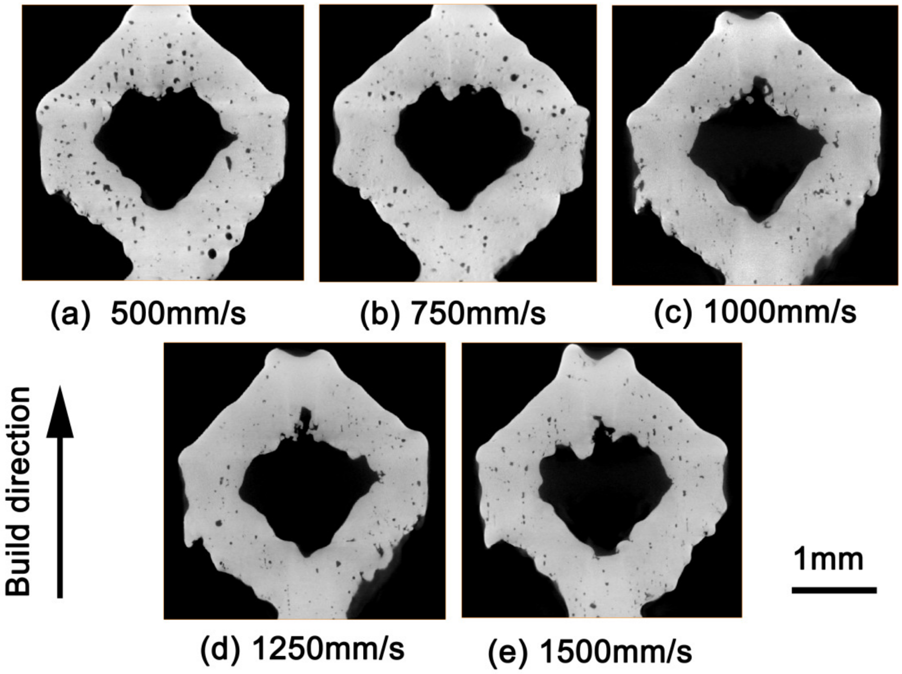

Fig. 3. Y.J. Liu *et al*

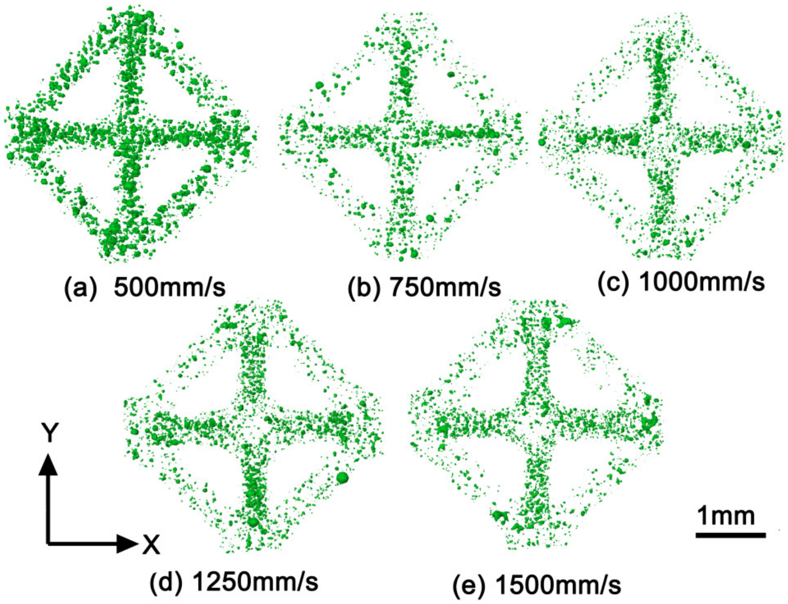

Fig. 4. Y.J. Liu *et al*

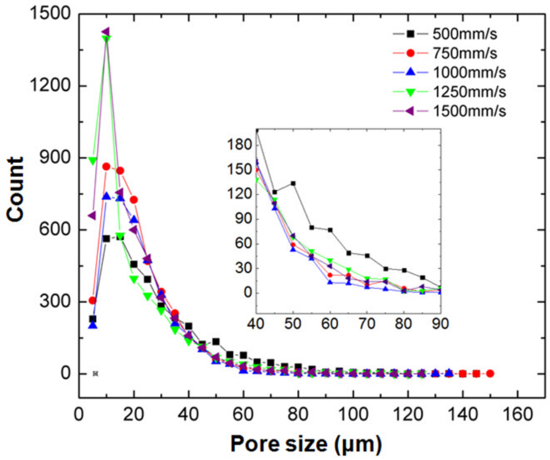

(a)

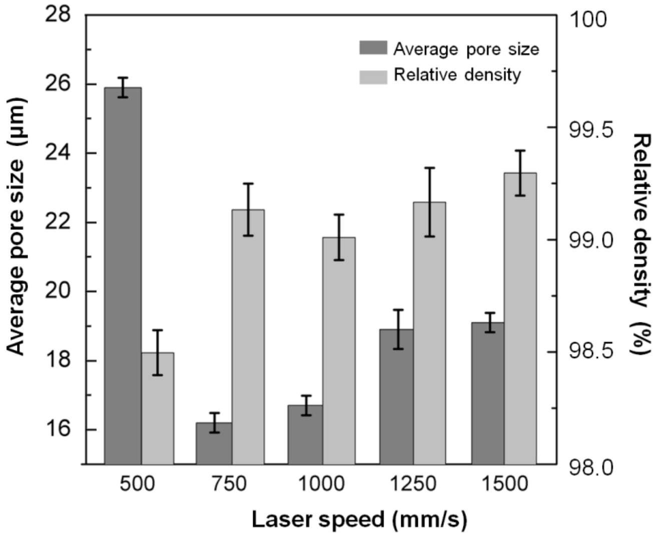

(b)

Fig. 5. Y.J. Liu *et al*

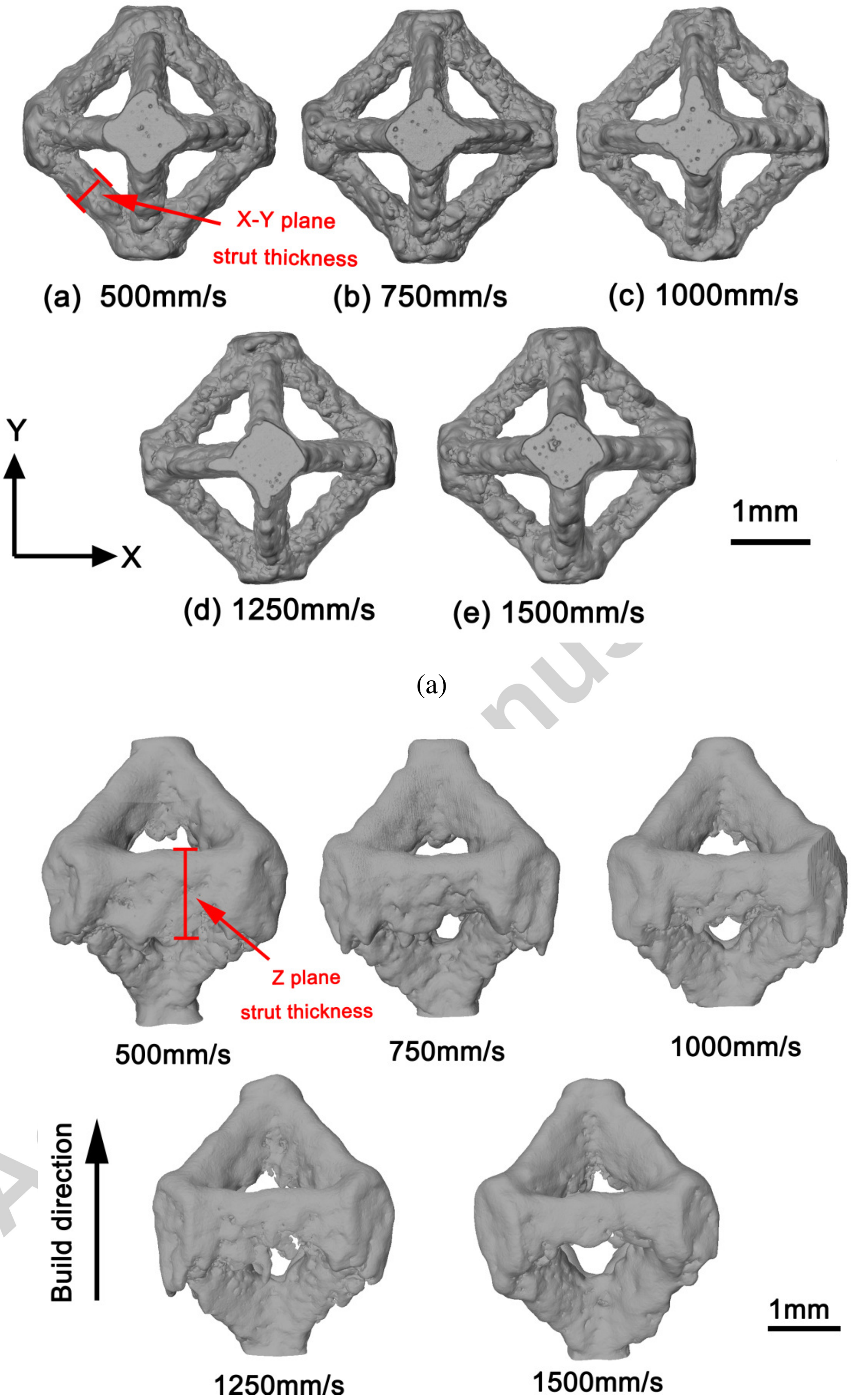

(a)

(b)

Fig. 6. Y.J. Liu *et al*

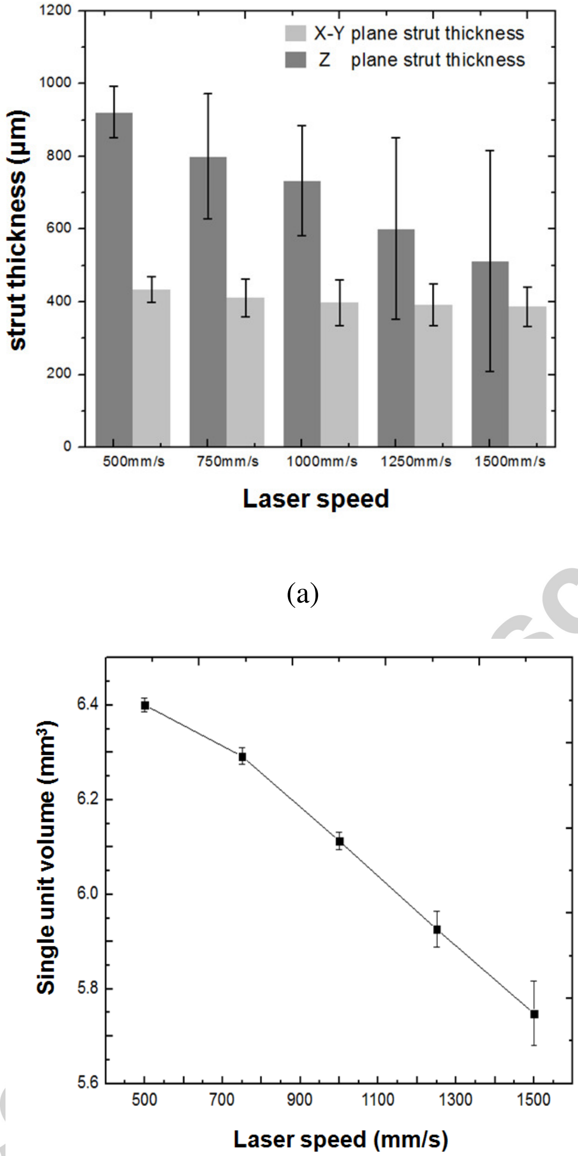

(a)

(b)

Fig. 7. Y.J. Liu *et al*

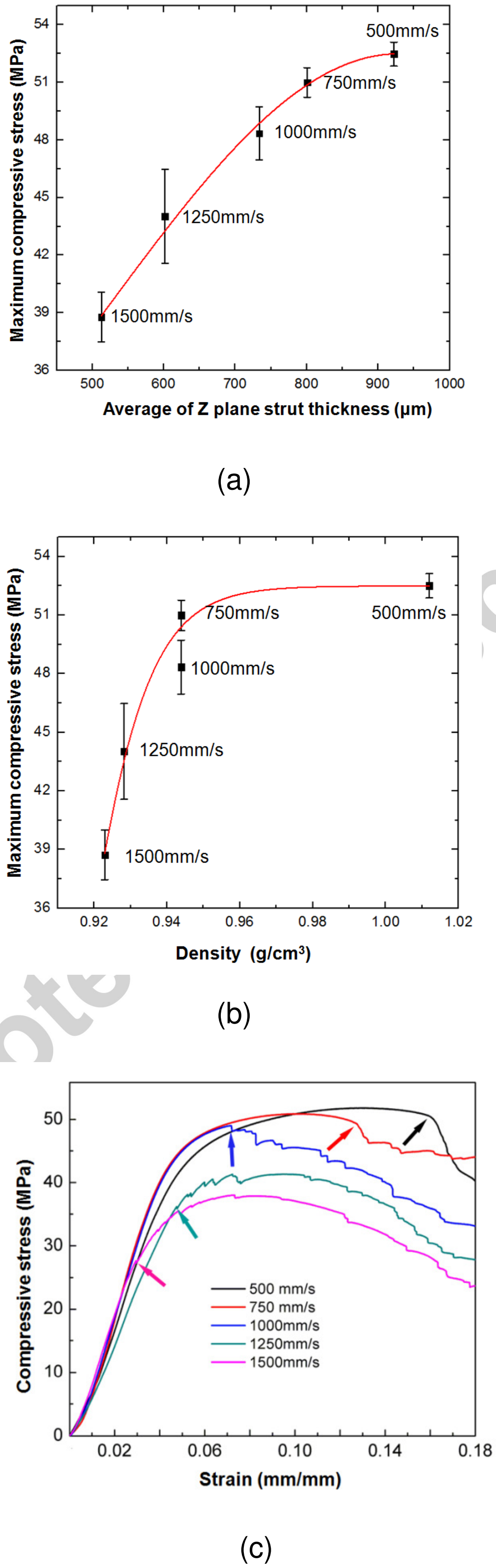

Fig. 8. Y.J. Liu *et al*

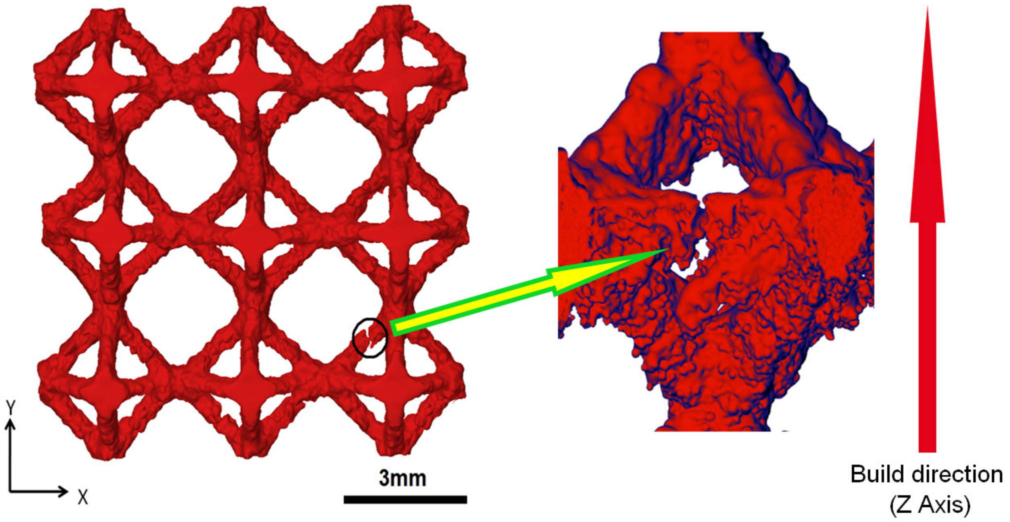

(a)Top view (b) Vertical view

Fig. 9. Y.J. Liu *et al*

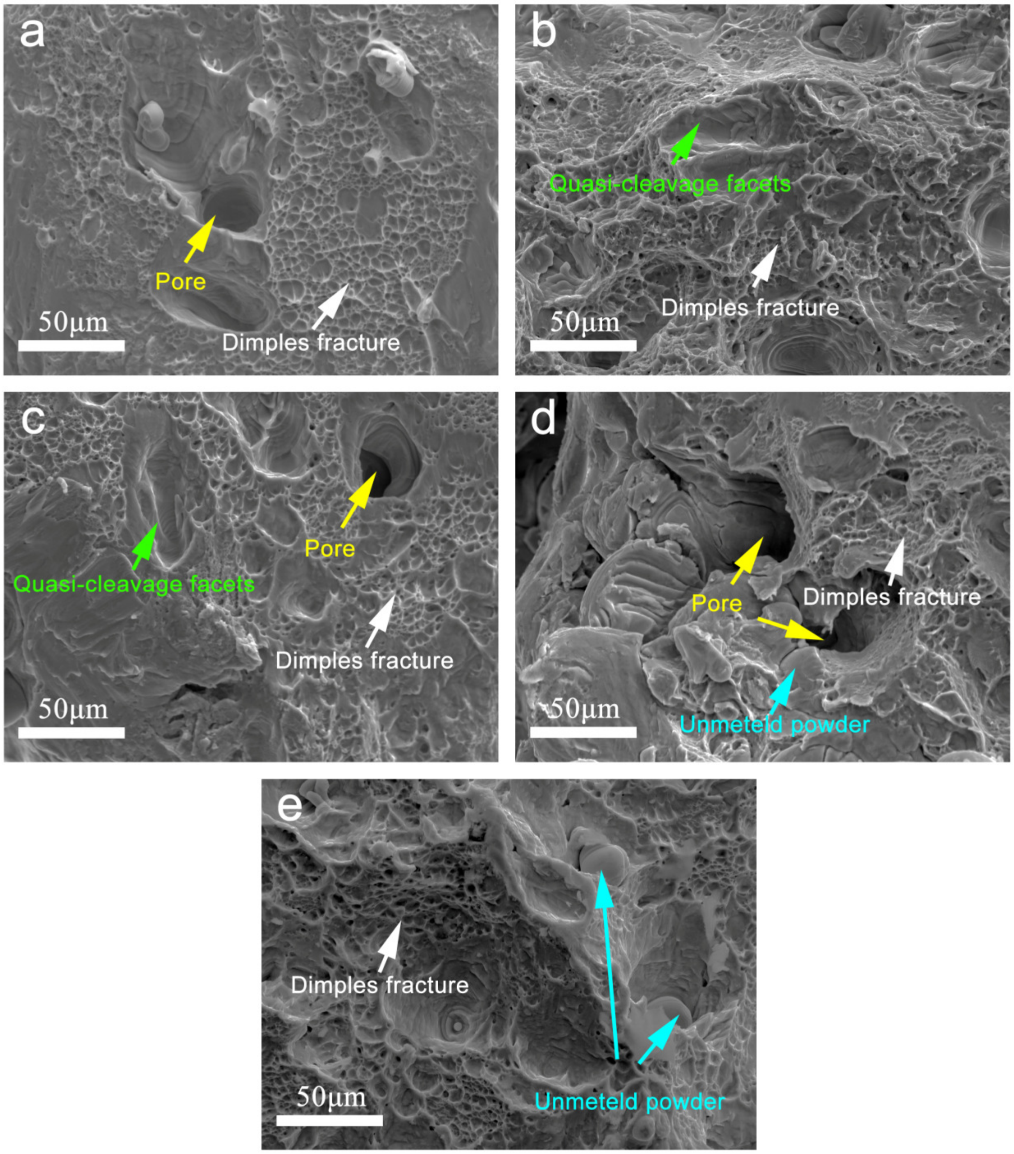

Fig. 10. Y.J. Liu *et al*